Provided for non-commercial research and education use.
Not for reproduction, distribution or commercial use.

This article appeared in a journal published by Elsevier. The attached copy is furnished to the author for internal non-commercial research and education use, including for instruction at the authors institution and sharing with colleagues.

Other uses, including reproduction and distribution, or selling or licensing copies, or posting to personal, institutional or third party websites are prohibited.

In most cases authors are permitted to post their version of the article (e.g. in Word or Tex form) to their personal website or institutional repository. Authors requiring further information regarding Elsevier's archiving and manuscript policies are encouraged to visit:

http://www.elsevier.com/copyright

Author's personal copy

Electrochimica Acta 75 (2012) 1–10

Contents lists available at SciVerse ScienceDirect

Electrochimica Acta

journal homepage: www.elsevier.com/locate/electacta

Probing the water content in polymer electrolyte fuel cells using neutron radiography

Jeffrey Mishler[a], Yun Wang[a,*], Rangachary Mukundan[b], Jacob Spendelow[b], Daniel S. Hussey[c], David L. Jacobson[c], Rodney L. Borup[b]

[a] Renewable Energy Resources Lab, Department of Mechanical and Aerospace Engineering, The University of California, Irvine, CA 92697-3975, USA
[b] Los Alamos National Laboratory (LANL), MS D429, MPA-11, Los Alamos, NM 87545, USA
[c] National Institute of Standards and Technology (NIST), Physical Measurement Laboratory, 100 Bureau Drive, MS 8461, Gaithersburg, MD 20899, USA

ARTICLE INFO

Article history:
Received 1 March 2012
Received in revised form 10 April 2012
Accepted 11 April 2012
Available online 8 May 2012

Keywords:
Polymer electrolyte fuel cell
Neutron imaging
PTFE loading
Channel configuration
Water profile

ABSTRACT

This work presents an in situ study on the water-content measurement in polymer electrolyte fuel cells (PEFCs) using neutron imaging. The effects of several important operating and design parameters on water content are examined, including the relative humidity (RH), the polytetraflouroethylene (PTFE) loadings in gas diffusion media including the microporous layer (MPL), current density, and flow field configurations including single-/quad-serpentine channels and co-/counter-flow configurations. Efforts are also made to distinguish water contents between the channel and land projected areas, and obtain the water profile along the gas flow path. We find that the highest water content occurs at a low current density for fixed operational stoichiometry, and liquid water emerges downstream at low humidity and increases rapidly after on-set.

© 2012 Elsevier Ltd. All rights reserved.

1. Introduction

Fuel cells convert the chemical energy in fuels directly and efficiently into electricity, which makes them low-pollution energy conversion devices, especially when compared with traditional combustion-based devices. Presently over 200 fuel cell vehicles, more than 20 fuel cell buses, and about 60 fuelling stations are operating in the United States. Approximately 75,000 fuel cells for stationary power, auxiliary power and specialty vehicles have been shipped worldwide, among them about 24,000 systems were manufactured in 2009, approximately a 40% increase over 2008 [1]. Polymer electrolyte membrane (PEM) fuel cells work at low operating temperatures and exhibit high power density, and are the primary type of fuel cell considered for portable and transportation applications.

A typical PEFC is composed of bipolar plates, gas diffusion layers (GDL) with micro-porous layers (MPLs), and a polymer electrolyte membrane with attached platinum catalyst layers, as shown in Fig. 1. Reactant gases are introduced in the gas flow channels and diffuse through the GDLs toward the catalyst layers. Protons are produced at the anode catalyst layer by the hydrogen oxidation reaction and are transported across the membrane. Oxygen is reduced in the cathode catalyst layer, combining with protons and electrons to produce water.

Water management is crucial to achieve high PEM fuel cell performance. Water in the membrane is essential for high electrolyte ionic conductivity, but excess water floods the catalyst layer and GDL [2–4], and can lead to gas-flow channel blockage [5,6], hampering reactant gas transport. Insufficient hydrogen and oxygen supply increases the mass transport polarization and hence voltage loss [7]. Comprehensive review on water management and transport in PEM fuel cells was provided by Wang [8], Weber and Newman [9], Jiao and Li [10], and Gurau and Mann [11].

Liquid water can emerge in operating PEM fuel cells [5,8,12] even at low-humidity operation [13]. Liquid water distribution is affected by many factors such as GDL structures [14], MPL properties [15–17], polytetrafluoroethylene (PTFE) loadings [18–24], operating conditions, and flow field configuration. Qi and Kaufman examined the fuel cell performance with various PTFE loadings in the GDL substrates and MPLs, and found MPLs can positively affect fuel cell performance [15]. Pasaogullari et al. developed a two-phase model to analyze the MPL's effect on water transport, indicating that MPLs promote anode water hydration, reduce cathode liquid level, and therefore relaxing mass transport limitations [25]. Weber et al. [16] developed an analytical model to examine the effect of the diffusion media's wettability on water management, demonstrating that MPLs are less susceptible to water flooding than the carbon substrate [17]. PTFE can be added to both GDL substrates

* Corresponding author. Tel.: +1 949 824 6004; fax: +1 949 824 8585.
E-mail address: yunw@uci.edu (Y. Wang).

0013-4686/$ – see front matter © 2012 Elsevier Ltd. All rights reserved.
http://dx.doi.org/10.1016/j.electacta.2012.04.040

Author's personal copy

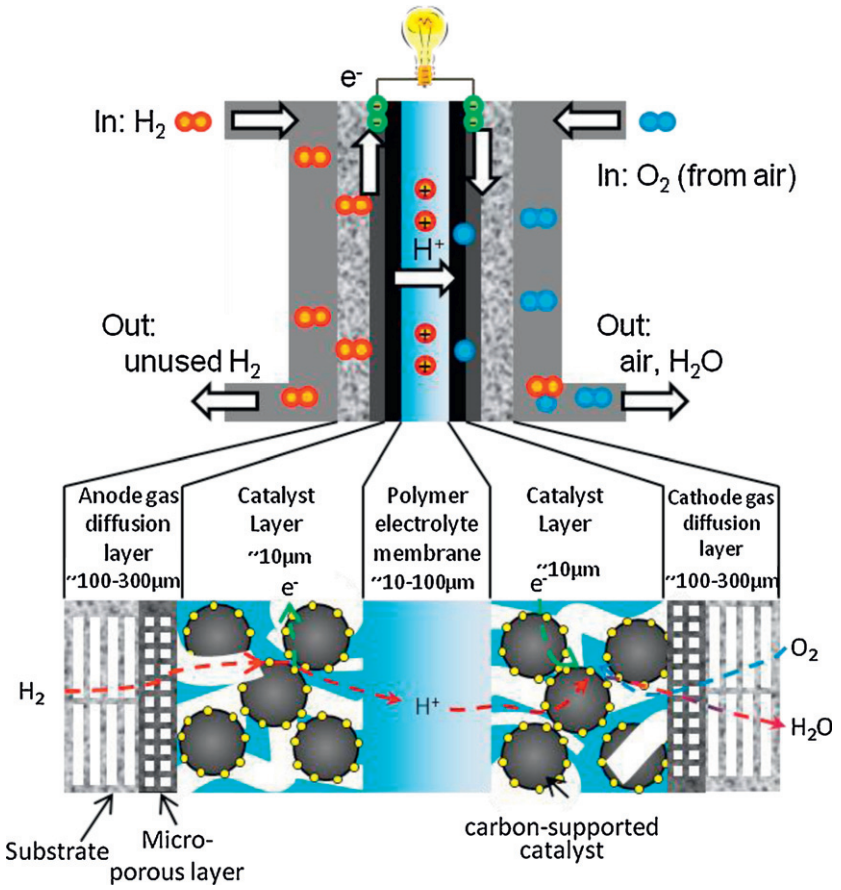

Fig. 1. Schematic of a polymer electrolyte fuel cell.

and MPLs to increase their hydrophobicity. Different optimal PTFE loading values have been shown in the literature, varying from 10% [18], 15% [19], 20% [20], to 30% in the substrate and 15% in the MPL [21]. Park et al. [22] performed water permeation experiments and indicated that adding PTFE can increase the water flow resistance in diffusion media, and that a PTFE loading of 23% provides effective water management. Wood et al. [23] examined the GDL PTFE loading's effects by using a segmented fuel cell. Wang and Chen [26] define a dimensionless parameter Da to characterize the flow regime in the GDL, i.e. single- vs. two-phase regimes: when $Da \to 0$, fuel cells are subjected to single-phase operation; while as $Da \to \infty$ there is full two-phase operation. A more precise expression was also explored for the dimensionless group at the channel central line.

In addition to diffusion media, flow fields distribute reactant gases and remove product water, therefore playing an important role in fuel cell water management. An overview of flow-field designs was provided by Li and Sabir [27]. Spernjak et al. [28] compared water content in 25 cm^2 fuel cells with parallel, serpentine, and interdigitated flow fields, and indicated the parallel flow field exhibits the highest water content but the worst performance, and the serpentine one shows the best performance and lowest water content. Wang et al. [29] envisaged the fuel cell channels as structured and ordered porous media, and further developed a continuum model of the two-phase channel flow. Wang developed a two-fluid model to examine the two-phase flow in the gas flow channels and obtained analytical solutions to liquid saturation, velocities, and pressure [30]. In flow field design, Owejan et al. [31] considered the flow channel's length and number. Murakawa et al. [32] studied single- and triple-serpentine flow-fields, indicating the average water content is higher in the triple serpentine channel. They also presented the water evolution for the single-serpentine flow field in the projected area of the channel and land area, respectively, showing higher water content in the channel projected area.

Neutron radiography has developed as a powerful tool for water in situ visualization and quantification in fuel cells. This is achieved by sending a beam of collimated thermal neutrons through a working fuel cell and measuring the attenuation of the transmitted neutrons [33]. The spatial and temporal resolution is determined by the neutron source and imaging set-up. The attenuated neutron beams are then captured by a detector. At the NIST Center for Neutron Research (NCNR), Sajita et al. [34] used a scintillating screen/CCD camera with per-pixel resolution of 100 $\mu m \times 100\ \mu m$ to perform 2D and 3D tomography, and indicated that the water under the land and channel areas was similar. Hickner et al. used a flat-panel amorphous-silicon detector with a per-pixel resolution of 127 $\mu m \times 127\ \mu m$ and an image capture rate of 1–30 frames/s. Using a 50 cm^2 fuel cell, they found water content is highly correlated with operating current density and cell temperature. They also presented a simple model to explain liquid water evaporation [35,36]. Their results indicated the maximum water content appears at a moderate current density, and the peak water content changes with temperature. Zhang et al. [37] also found the maximum water content occurs in a moderate current. Park et al. [38] and Owejan et al. [39] used serpentine flow fields set perpendicularly to each other to distinguish water in the areas of the anode and cathode lands and channels, respectively. Owejan found the channel geometry and surface tension can affect water accumulation. Park indicated that water accumulates in the GDL region adjacent to gas flow channel, while water under lands seems to be effectively removed. Kim et al. [40] examined

Author's personal copy

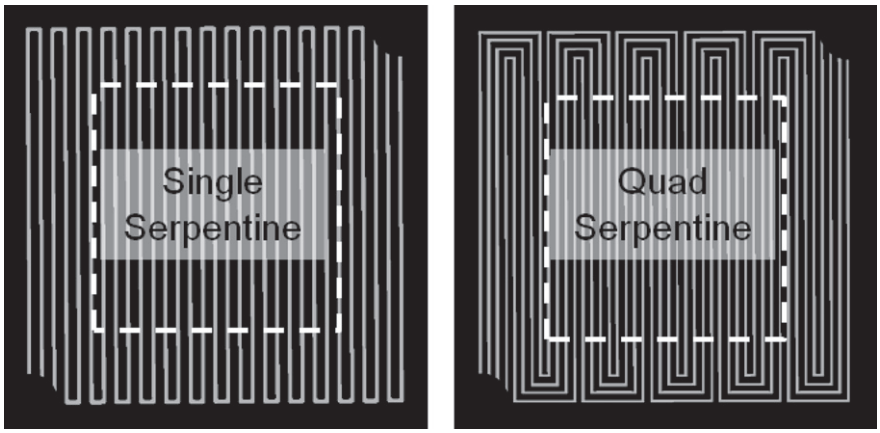

Fig. 2. The two flow fields used in the study: the single-serpentine (left) and quad-serpentine (right). The dotted line shows the analysis region.

Table 1
GDL/MPL configurations of the tested fuel cells.

Cell #	Flow field type	PTFE loading (wt%)			
		Anode substrate	Anode MPL	Cathode substrate	Cathode MPL
1	Single serpentine	5%	23%	20%	10%
2	Single serpentine	5%	23%	5%	23%
3	Quad serpentine	5%	23%	20%	10%
4	Single serpentine	5%	5%	20%	10%

flow direction with three-parallel serpentine flow fields, indicating different water characteristics but nearly identical performance between the co- and counter-flows. Mukundan et al. [24] used high-resolution neutron radiography to probe the water distribution in the through-plane direction, indicating that more water appears on the anode side when the cathode MPL has higher PTFE loading. Water will freeze under subfreezing temperature, and Mukundan et al. [41] and Wang et al. [42] measured water content at −10 and 20 °C using neutron imaging, showing ice accumulation with time under channel and land, respectively.

At the Paul Scherrer Institute, Kramer et al. employed neutron imaging to study the water amount in GDLs, finding that about 30% of the GDL pores were not filled with liquid water [43]. Zhang et al. reported more water in carbon paper GDLs relative to carbon cloth, and also established various water removal regimes: the first third of the flow channel is dominated by evaporation, whereas the remainder is dominated by droplet removal [37]. Yoshizawa et al. [44] found more water content for carbon cloth GDLs in comparison with carbon paper for straight flow fields. They used neutron radiographs as a guide for improving flow field design. Schneider et al. found that for co-flow operation it was possible for a portion of a fuel cell to be flooded while other parts to be dry [45]. A technique was later used to measure the local current and liquid water profile. They indicated higher current appears in the channel areas and lower in the land areas due to the longer oxygen diffusion path to the reaction sites under the land [46], and that this nonhomogeneity is more prevalent at higher current densities [47].

Despite previous neutron imaging efforts, an extensive study of the water content in fuel cells such as the water contents under land and channel, and the effects of various PTFE loadings and flow configurations, are still highly needed. This kind of knowledge is important to both fundamental understanding of water transport and optimization of fuel cell design and operating condition. In this paper, we will provide an extensive neutron radiography study that examines the effects of several important factors, including different relative humidity (RH), current density, PTFE loading in GDLs and MPLs, flow field design, and flow pattern. Both co- and counter-flow configurations, and single-channel and quad-serpentine flow fields are compared.

2. Experimental

2.1. Fuel cell testing

The fuel cell hardware was designed specifically for neutron imaging at the NIST, and was custom built at Los Alamos National Laboratory. The experimental fuel cells have an active area of 50 cm^2 with gold-plated aluminum bipolar plates to prevent corrosion at the GDL-bipolar plate interface, and a furon pressure plate between the end plates and current collectors to improve the contact of flow fields to GDLs. Two different flow fields are used, they are single- and quad-serpentines (see Fig. 2). The former has a channel length of 2.2 m, whereas the latter has 0.78 m, with a cross-section of 1.11 mm wide and 1.0 mm deep, and a land dimension of 1.16 mm. The MEA was a Gore[1] Primea MEA Series 57 with 18 μm thick GORE-SELECT membrane with carbon supported 0.2 mg Pt cm^{-2} on the cathode and 0.1 mg Pt cm^{-2} on the anode (GORE-SELECT, PRIMEA and GORE are trademarks of W.L. Gore & Associates, Inc.). The gas diffusion media were SGL carbon paper 24-series with a 200 μm thick substrate and a 50 μm thick MPL. Table 1 summarizes the configurations of MPLs and GDLs in the experiment.

The fuel cells were operated at 80 °C, with anode hydrogen and cathode air stoichiometries of 1.2 and 2.0 and minimum flow rates of 50 sccm and 75 sccm (standard cm^3 min^{-1}), respectively. Two inlet-flow RHs were examined: low humidity (50%) and full humidification (100%). Most measurements were performed in a co-flow

[1] Certain trade names and company products are mentioned in the text or identified in an illustration in order to adequately specify the experimental procedure and equipment used. In no case does such identification imply recommendation or endorsement by the National Institute of Standards and Technology, nor does it imply that the products are necessarily the best available for the purpose.

Author's personal copy

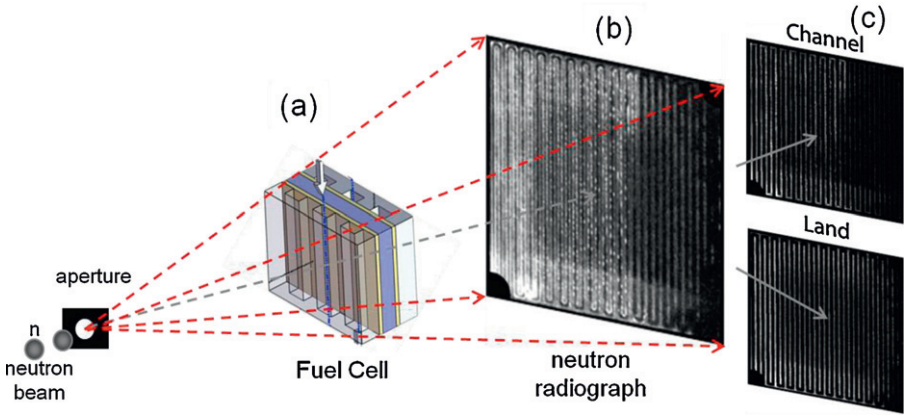

Fig. 3. Schematic of neutron imaging. Neutron beams are directed through an operating fuel cell (a) toward a CCD where a neutron radiograph is recorded (b). Masks can be applied to analyze water contents in the projected areas of channels and lands (c).

configuration, where hydrogen and air reactants flow in the same direction, with additional measurements made for counter-flow configuration for comparison purpose. The outlet gas backpressure was set to 172 kPa absolute (25 psi).

Testing was carried out at constant current density and five currents ranging from 0 to 1.6 A/cm^2 in intervals of 0.4 A/cm^2 (i.e. 0 A/cm^2, 0.4 A/cm^2, 0.8 A/cm^2, 1.2 A/cm^2, 1.6 A/cm^2). Measurements were made after the fuel cells reached steady state. Steady state was achieved by setting a current density and then running for at least 15 min or until the voltage was stabilized. Each measurement was taken for at least 30 min, during which time the standard deviation of the current density was less than 0.001 A/cm^2, and that of the voltage was about 0.01 V. Data was obtained at all current densities for 50% anode/50% cathode inlet RH, but only at a limited number of current densities for 100% anode/100% cathode inlet RH due to limited neutron beam time availability.

2.2. Neutron imaging

Neutron imaging was performed at the National Institute of Standards and Technology (NIST) Center for Neutron Research (NCNR) using the thermal beam tube 2. The sensor used was an amorphous silicon detector with approximately 250 μm resolution (pixel dimension of 127 μm × 127 μm) [48]. Fig. 3 shows a schematic of applying neutron radiography to probe water distribution inside a fuel cell. After the radiograph was recorded, analysis is performed based on the Lambert–Beer law of attenuation, as described by Trabold et al. [33]

$$I = I_o e^{-N\sigma T} \tag{1}$$

where I is the intensity of the transmitted neutrons (those that make it entirely through the sample), I_o the intensity of the incident neutrons (those hitting the sample), N the atomic density of the material through which they pass, σ the neutron cross-section, and T the thickness of the neutron beam attenuating medium. A fuel cell consists of several component materials, therefore a summation can be taken to express the intensity:

$$I = I_o e^{-\sum_i (N\sigma T)_i} \tag{2}$$

where i represents each of the materials in a fuel cell. In order to isolate the attenuation by only the water we record one radiograph of the fuel cell when dry, I_{dry}, and another while running the fuel cell, I_{wet}. Dividing one by the other cancels out the attenuation of all materials except for the water:

$$\frac{I_{wet}}{I_{dry}} = e^{-(N\sigma T)_{H_2O_{(l)}}} \tag{3}$$

Rearranging the equation, and defining $\mu_w = N\sigma$ as the water attenuation coefficient, we can solve for the water thickness T:

$$T = \frac{-1}{\mu_w} \ln\left(\frac{I_{wet}}{I_{dry}}\right) \tag{4}$$

The water attenuation coefficient μ_w is experimentally determined by use of a specially manufactured cuvette of known water thicknesses and measuring the incident neutron intensity [48]. Analysis as described above was performed using the IDL programming language, with an example of the resulting radiograph shown in Fig. 3(b).

Like all imaging technologies, neutron radiography resolution is influenced by the scattering of the signal on its path to the sensor. This shows up in imagery as a blurring of the data, known as a point-spread function, as described by Hussey [49]. For this study, this represents an error of about 0.3%.

Masks were made to distinguish the projected land and channel areas, see Fig. 3(c). For the pixels in the boundary area between the channel and land areas, the resolution makes it difficult to cleanly determine the proportions of detected water from the projected channel or land region, therefore we chose to exclude these pixels as either land or channel. The channel and land masks cover the middle of the channel and land area, bounded by the pressure plate. The active area mask covers the middle of the fuel cell, including the channel and land areas and the above-mentioned boundary area (~20%). The masks were further broken down into five segments to determine the along-channel distribution of water in the fuel cells. In order to obtain neutron images, 60 exposures per minute were taken and further averaged into a single image. For each operating condition at least thirty 60 s intervals were acquired, and then averaged to get the average steady-state water content in the fuel cell. In addition, to diminish the effects of side boundaries, U-turns, and inlet/outlet regions, the imaging analysis is focused on the fuel cell's central region with an area of 4.6 cm × 4.6 cm, as shown by the dotted line in Fig. 2. The water contents and their profiles are obtained by averaging the probed water over the central region or its segments.

The random uncertainty of the water content from the neutron radiography is discussed in detail by Hussey et al. [48]. For cases in which the fuel cell does not have uniform water content, as in this

Author's personal copy

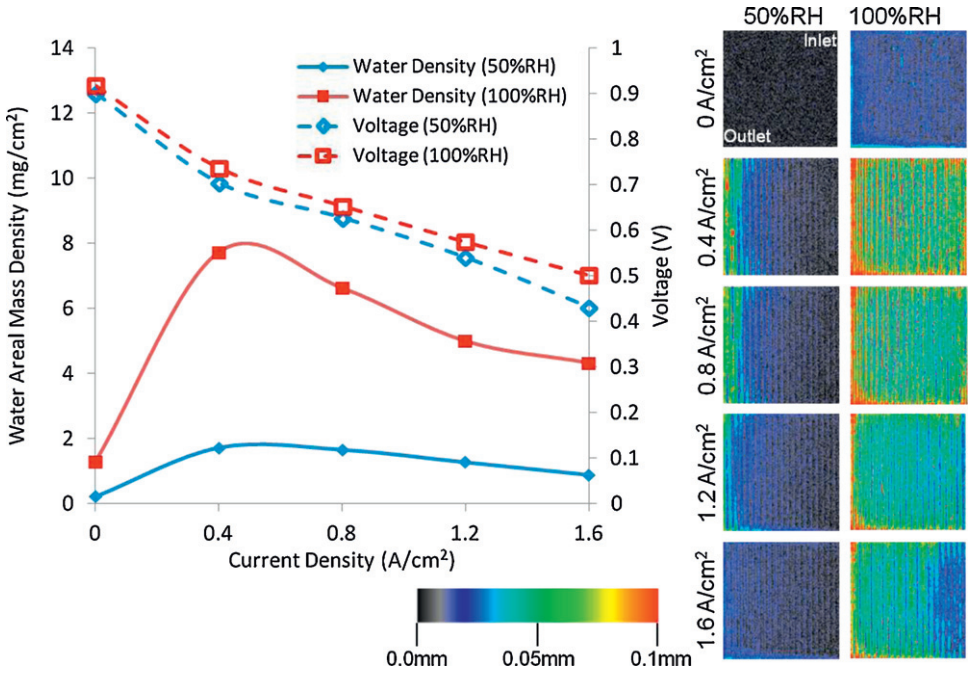

Fig. 4. Water areal density and performance of cell #1 at inlet relative humidities of 50% and 100%, respectively, (left); the corresponding false colored neutron images, with scale (right). For the neutron images, the gas inlets are in the top-right, and gas outlets are in the bottom-left. (For interpretation of the references to color in the text, the reader is referred to the web version of the article.)

study, the root mean square deviation of the water distribution gives a reasonable estimate of water uncertainty. This value was under 1% of the water areal density for most tests, sufficiently small to be visible in the figures.

3. Results and discussion

3.1. Inlet gas flows with different relative humidities

Fig. 4 shows the average water density over the active area and the performance at each operating condition for cell #1, running at 50% and at 100% inlet RHs, respectively. The right side of Fig. 4 shows false colored neutron images of the water contents, with a corresponding scale used for all colored images presented. Darker colors (black, gray, and blue) represent areas of low water density, and lighter colors (yellow, red) represent areas of higher water density. For all images presented in this paper, the gas flows enter the fuel cell in the top-right corner and exit in the bottom-left corner. At zero current, a small amount of gas is still fed in (50 sccm and 75 sccm) at the anode and cathode, respectively. At the current density of zero when no water is produced, the 50% inlet RH case shows almost zero water content due to the fact that the fuel cell is not yet saturated and therefore no liquid water is present, while the 100% inlet RH case clearly shows a considerable amount of residual liquid water, s_{ir}. The irreducible residual saturation is the liquid fraction bound inside capillary channels or pores by surface tension forces and cannot be removed by drainage but only by evaporation. Saez and Carbonell [50] calculated the irreducible residual saturation for mini-channels:

$$s_{ir} = \frac{1}{20 + 0.9\text{Eö}} \tag{5}$$

where the Eotovos number Eö is defined as:

$$\text{Eö} = \frac{\rho_1 g d_h^2}{\sigma} \tag{6}$$

where ρ_1 is the fluid density, g is gravitational acceleration, d_h is the hydraulic diameter of the channel, and σ is surface tension. For the given conditions the s_{ir} was calculated to be about 4.9% in a gas

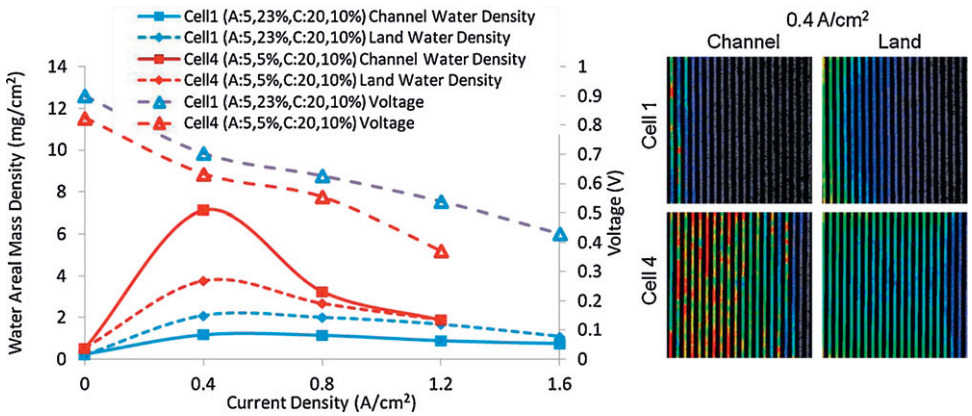

Fig. 5. Water areal density under the lands and channel at 50% RH for different MPL configurations (left); the corresponding colored neutron images at 0.4 A/cm² (right).

Author's personal copy

flow channel. Given the parameters of the fuel cell hardware, we would expect the irreducible water content within the channels to be 0.6 mg/cm^2. Experimental results for each fuel cell running at open circuit voltage and 100% RH inlet flows show the water ranging from 1.3 mg/cm^2 for cell #1 to 4.2 mg/cm^2 for cell #2, which, when also considering the liquid in the GDL and in the membrane, is of the same order. At 50% inlet RH, the dry gases evaporate the liquid water, resulting in no residual liquid water present at steady state. Such an evaporation process is usually limited by transport in the diffusion media [51]. Residual liquid water was also observed by Hickner et al. [36] in their neutron radiographs. At conditions of 80 °C, 100% inlet RH, and 1500 sccm anode flow rate and twice the stoichiometric cathode flow rate required for 0.01 A/cm^2, Hickner's results showed 8.2 mg/cm^2 of water at open circuit voltage (OCV), considerably higher than the results found here. In addition, with the exception of cell #2, the highest overall water content level for the fuel cells appears at the low current density of 0.4 A/cm^2 (compared to at 1.2 A/cm^2, 35% more water for cell #1, 29% more for cell #2, and 2.3 times and 1.7 times as much water in cells #3 and #4; cell #2 had slightly higher (17%) water content at 0.8 A/cm^2). This is likely due to the fact that the cases with higher current densities have higher volume flow rates in flow channels, which are more effective in removing the liquid water in channels. Wang et al. [29] showed that when the stoichiometry is reduced the fuel cell operation becomes unstable due to the inefficient liquid water removal by gas flows. This agrees with prior neutron imaging studies [33]. In addition, high current operation produces more waste heat, which can evaporate liquid water in the GDL, as pointed out by Wang et al. [14] and Hickner et al. [35].

3.2. Land vs. channel projected regions

Fig. 5 presents the water contents in the land and channel projected areas, respectively, along with the corresponding masked neutron images for the 0.4 A/cm^2 current density case. Note that the presented water contents in the projected land area include the water in both GDLs and the MEA, and those in the projected channel area additionally includes water in the gas flow channels.

For cell #1, the land area has a higher water content at operation, which is likely due to the larger transport resistance. When a less hydrophobic anode MPL is used, such as in cell #4, there is a large difference in the water content under the channel and land areas at 0.4 A/cm^2. One possible reason is that more water appears to be forced back to the anode because of its less hydrophobic MPL, and hence the anode channel flooding becomes severe in cell #4.

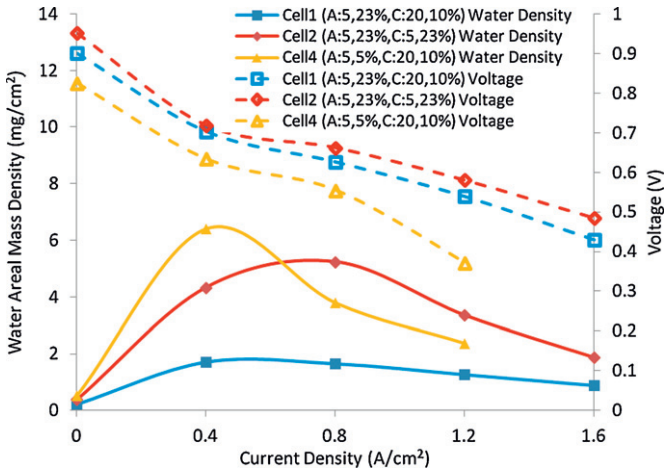

Fig. 6. Water areal density and cell performance for different PTFE loadings in the GDL substrate and MPL at 50% inlet RH.

In particular at the current density of 0.4 A/cm^2, the gas flow rate is slow, especially on the anode side, resulting in inefficient liquid removal and hence water accumulation in the channel. At higher currents where the anode flow rate becomes stronger, the anode channel water can be removed more efficiently, bringing the water contents in the two areas closer. Two-phase flow on the anode side has been explained by Ge and Wang [52] and Wang [13].

3.3. Various PTFE loadings in GDLs and MPLs

Compared to cell #1, cell #4 has a lower PTFE loading in the anode MPL, and cell #2 has different PTFE loadings in the cathode GDL and MPL. Both cell performance and water content change when altering the wettability of GDLs or MPLs. In particular, an improvement in cell performance is indicated when increasing the PTFE loading in the anode MPL from 5% (triangles or cell #4) to 23% (squares or cell #1), as shown in Fig. 6. Also higher water content is observed in cell #4 at 0.4 A/cm^2, which can be explained by its less hydrophobic anode MPL (resulting in more water driven to the anode side via the membrane). More water in the anode can cause the anode channel flooding, which can be severe at 0.4 A/cm^2 due to the corresponding low gas flow rate. Likewise, compared to cell #1, cell #2 has a more hydrophobic cathode MPL, forcing more water from the cathode to the anode side. With increasing current density, the anode channel flooding can be alleviated through increased electro-osmotic drag and gas flow rates, and the water contents in both cell #2 and #4 are found to decrease rapidly. In addition, cell #2 has more hydrophobic MPLs in both anode and cathode, therefore the water transport barrier across the MPLs is higher, leading to a more hydrated MEA, as can be seen by looking at the high frequency resistance (HFR) shown in Table 2, and hence reduced ohmic loss. This may be one major cause for the higher performance of cell #2. The MPL's effect is consistent with the model analysis by Pasaogullari et al. [25] and Weber et al. [16], and the through-plane radiography by Mukundan et al. [24]. Further, at 1.2 A/cm^2, cell #4 displays a rapid drop in cell performance though its averaged water content is less than that of cell #2. This can be possibly explained using the same facts as stated above: cell #4 is subject to anode flooding due to its less hydrophobic anode MPL. The liquid water in the anode hampers hydrogen supply, limiting the current density. As to cell #2, its more hydrophobic MPLs result in a better hydrated membrane in a larger area of the fuel cell (note that part of the fuel cell is dry due to the 50% RH inlet condition), therefore it performs better and yields a higher averaged water thickness.

3.4. Single- vs. quad-serpentine flow fields

Fig. 7 displays the average water density and performance for fuel cells with single- and quad-serpentine flow fields with the same GDL configuration as cell #1. The quad-serpentine cell exhibits higher water contents than the single serpentine cell except at the highest tested current density of 1.6 A/cm^2 for the channel projected area and 1.2 A/cm^2 and 1.6 A/cm^2 for the land. For 0.4 A/cm^2 and 0.8 A/cm^2, the water content for quad-serpentine flow fields is much higher (about twice for the land area) than that of the single-serpentine flow field (3.2 mg/cm^2 vs. 1.7 mg/cm^2 for 0.4 A/cm^2 and 3.7 mg/cm^2 vs. 1.7 mg/cm^2 for 0.8 A/cm^2). The latter has a longer channel length in one flow path, therefore the reactant flow velocity is much higher than that in the quad-serpentine flow field. The higher gas velocity benefits the water removal in the gas flow channels, leaving much less water accumulation in the channel region. With increasing current density, the channel gas flow rate increases, reducing the water content in the quad-serpentine fuel cell. Two-phase transport in gas flow channels has

Author's personal copy

Table 2
High frequency resistance of the tested fuel cells.

Current (A/cm^2)	High-frequency resistance (Ω cm^2)			
	Cell #1 (A: 5%, 23%; C: 20%, 10%)	Cell #2 (A: 5%, 23%; C: 5%, 23%)	Cell #3 (A: 5%, 23%; C: 20%, 10%)	Cell #4 (A: 5%, 5%; C: 20%, 10%)
	50% inlet RH			
0.4	0.062	0.046	0.055	0.044
0.8	0.057	0.040	0.051	0.058
1.2	0.057	0.041	0.059	0.056
1.6	0.064	0.043	0.080	–
	100% inlet RH			
0.4	0.042	–	0.039	0.041
0.8	0.042	–	0.038	0.041
1.2	0.042	0.039	0.039	–
1.6	0.043	0.039	0.039	–

	Cell #1 (A: 5%, 23%; C: 20%, 10%)		
	Co-flow, 50% inlet RH	Co-flow, 100% inlet RH	Counter-flow, 50% inlet RH
0.4	0.062	0.042	0.045
0.8	0.057	0.042	0.045
1.2	0.057	0.042	0.046
1.6	0.064	0.043	0.050

been theoretically analyzed by Wang et al. [29,53] and Wang [30]. For dry operation, the mass transport polarization is relatively unimportant as opposed to the ohmic loss at moderate current densities, therefore the performance of the quad-serpentine fuel cell is slightly higher than the single-serpentine one due to the better membrane hydration and hence ionic conductivity. At the current density of 1.2 A/cm^2, the quad-serpentine fuel cell has lower water content under the land, and hence lower cell performance. At the highest current density of 1.6 A/cm^2, the single-serpentine fuel cell has higher contents in both land and channel areas, and a better performance of 0.43 V, while the quad serpentine one is 0.08 V. The increased water content of the single-serpentine configuration relative to the other configuration is likely due to the water accumulation arising from the reactant bypass flow through the GDL under lands: such bypass flows occur near the U-turns and are severe for the single-serpentine due to the fast gas flow rate, and can significantly reduce the gas velocity in the part of the channels away from the U-turns, as explained by Wang and Wang [54]. Note that the waste heat production by fuel cells at this high current can subject the cells to dry operation, thus the ohmic voltage loss can be significant. For the quad-serpentine, no water accumulation occurs in such a way because the channels are in parallel and little pressure difference appears between two adjacent channels, and the consequent dry membrane and large ohmic resistance (increase in HFR of 36% from 1.2 A/cm^2 to 1.6 A/cm^2, as shown in Table 2) lead to almost operation failure.

Another interesting result is the opposite trends between the two flow fields in terms of the water thickness difference between the projected land and channel areas: the water accumulation under land is always greater than that under channel in the single serpentine case, whereas an opposite trend is observed for the quad serpentine. This can be explained using the same fact we present above for channel two-phase flow: the gas flow rate in the gas flow channels of the quad serpentine flow field is much lower than that of the single serpentine, yielding a weaker capability of liquid water removal in the flow channels for the quad serpentine

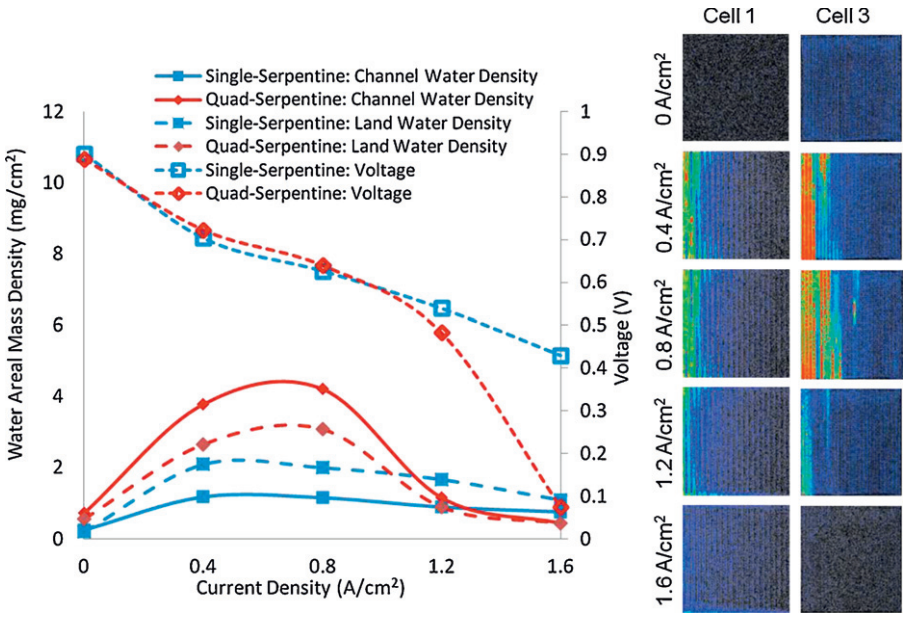

Fig. 7. Water areal density and performance for fuel cells with single- and quad-serpentine flow fields, respectively, at 50% inlet RH (left); the corresponding colored neutron images (right) (the PTFE loadings: anode side 5% substrate, 23% MPL; cathode side 20% substrate, 10% MPL).

Author's personal copy

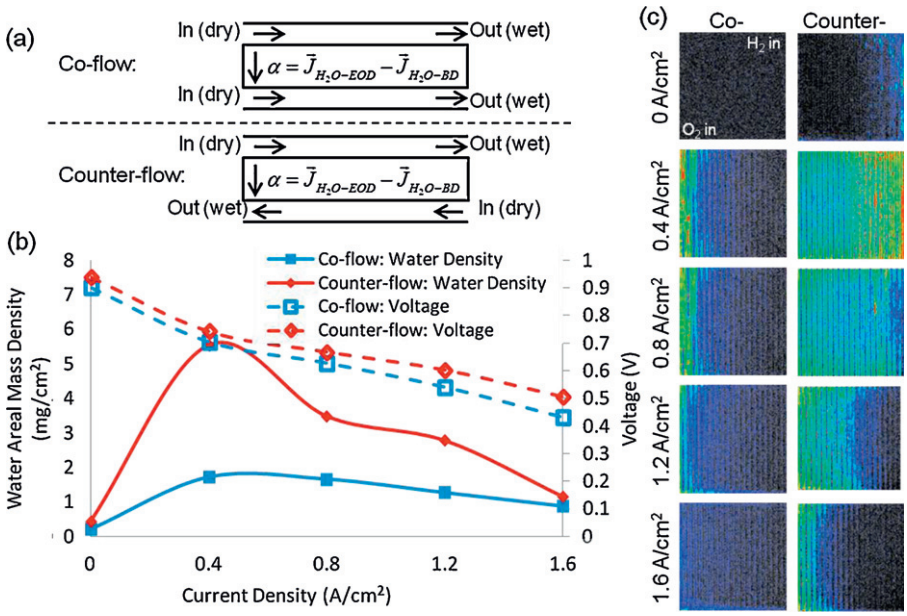

Fig. 8. Schematic of flow configurations for co-flow and counter-flow operation (a), water areal density and performance for cell #1 with different flow configurations at 50% inlet RH (b); the corresponding colored neutron images (c).

case. Note that gas flow channel can contain a large amount of liquid water comparing with other components. As a result, more water is accumulated in the projected channel region as opposed to the land area for the quad serpentine. As to the single serpentine, its much faster gas flows in channels yield more effective liquid water removal and hence a lower water thickness in the projected channel region comparing with the land region.

3.5. Co-flow vs. counter-flow configurations

Fig. 8 presents the average water areal density and performance for cell #1 running under different flow configurations. In the counter-flow configuration, as shown in Fig. 8(a), the inlets for the hydrogen and air are on the opposite sides of the flow path. This creates a larger water concentration gradient across the MEA at the operating condition, and further promotes the water recirculation between the cathode and anode sides, i.e. internal humidification as described by Büchi and Srinivasan [55]. The internal humidification results in better hydrated MEA and hence better performance (Fig. 8(b)). In addition, more water appears on the anode side. This is especially severe at the low flow velocity of 0.4 A/cm^2, leading to a large difference in water content between the two configurations, 5.5 mg/cm^2 for the counter-flow configuration and 1.7 mg/cm^2 for the other. As current density increases, the difference diminishes.

The neutron images of each of the flow fields (Fig. 8(c)) show that in addition to a higher integral water content with counter-flow operation, as also shown by Kim et al. [40] there appear distinct water distributions between the two configurations. The chart on the right side of Fig. 10 quantizes this, showing the water distribution along the flow channel path for the co-flow and counter-flow operation of cell #1. For the counter flow, a large water content near the inlet for the low current density of 0.4 A/cm^2, comparable to the water distribution at 100% inlet RH shown on the left side of Fig. 10 (segment #1). At higher current densities, the liquid water area becomes smaller for both cases, indicative of dryout by the larger amount of waste heat generation of fuel cells. Due to the internal humidification, the counter flow shows a much larger liquid water region.

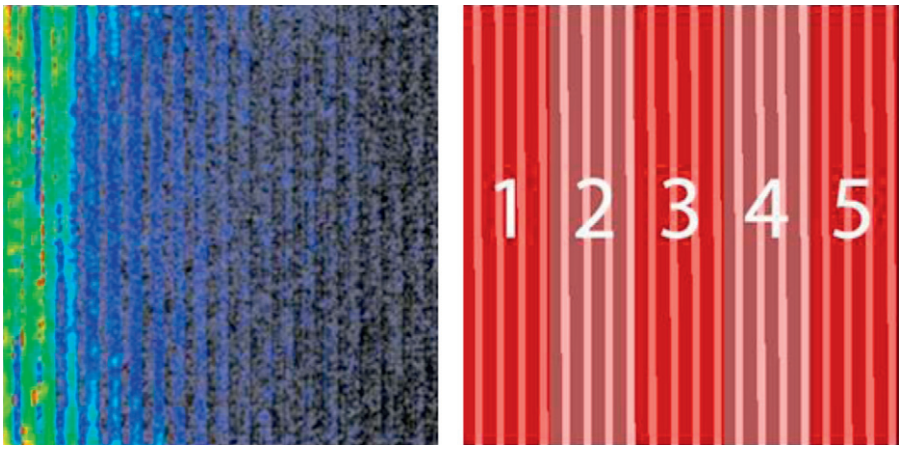

Fig. 9. Water density images at 50%/50% RH and 0.8 A/cm^2 for cell #1 (left) and segmenting diagram for the single-serpentine flow field (right).

Author's personal copy

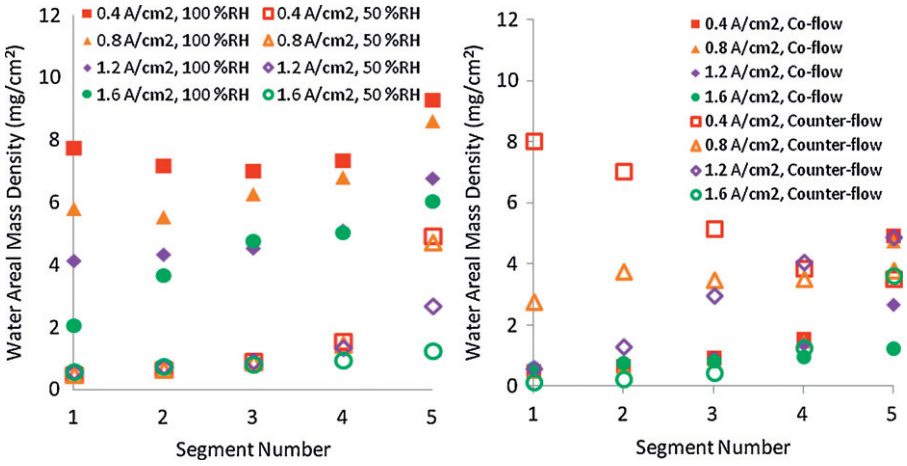

Fig. 10. The water areal density profiles along the flow channel for cell #1 at the inlet RH of 50% and 100%, respectively, and operating in co-flow configuration (left), and operating at co-flow and counter-flow for inlet RH of 50% (right).

3.6. Water profile along gas flow channels

The neutron images of the water content for cell #1 at 0.8 A/cm^2 are shown in Fig. 9. In order to obtain the water profile along the flow channel, the mask was divided in to five regions from the inlet to the outlet, as seen on the right side of Fig. 9, and the averaged water contents over each of the segments, respectively, represent a water profile along the channel. The water profiles at different RHs are shown on the left side of Fig. 10, while the right side presents the water evolution along the flow length for co-/counter-flow configurations. Fig. 10 shows a gradual increase in water content at the beginning for 50% inlet RH for most cases except the highest current until the 3rd segment, where the liquid content starts to change rapidly. For the 100% RH case, liquid water is high near the inlet, indicating a rapid increase in liquid content between the inlet and segment #1. Wang [30] reported a formula to predict the onset of two-phase flow in flow channels:

$$\bar{x}^* = \left(\frac{\xi_c \rho_g}{2C_{g,in}^{O_2}}\right) \frac{C_{g,sat}^{H_2O} - C_{g,in}^{H_2O}}{(1+2\alpha)\rho_g - 2C_{g,sat}^{H_2O}\left(\frac{1}{2}M^{H_2} + \alpha M^{H_2O}\right)} \tag{7}$$

where ξ_c is the cathode side stoichiometric flow ratio, ρ_g the gas density, C the species concentration, M the molecular weight, α the net water transport coefficient, and $\bar{x}^*$ the along-channel dimensionless location where liquid water first appears. Additionally, the liquid saturation can be calculated by:

$$s_l = \frac{(u_l\mu_l/u_g\mu_g)^{1/n_k} + s_{ir}}{1 + (u_l\mu_l/u_g\mu_g)^{1/n_k}} \tag{8}$$

where u_l and u_g are the superficial velocities of the liquid and gas phases, respectively, and μ_l and μ_g the viscosities of the liquid and gas phases, and n_k the exponent in the relative permeability. The relative permeability of the liquid water saturation, as described by Hilfer [56]. In fuel cells, some studies have adopted a value of 3 or 4 for n_k, indicating liquid water substantially affects the gas flow. For the case of uniform current density Wang calculated with Eq. (8) that the liquid water onset in the channel occurs around 55% down the length of the channel for the inlet RH of 50%, and at the beginning of the channel for the inlet RH of 100%, and channel liquid increases its content rapidly thereafter. This is consistent with the present experimental observation. Fig. 10 (right) plots the water profiles in the counter-flow configuration.

In addition, for the co-flow configuration there is a drop in water content from segment 1 to 2 at low current densities for fully humidified cases. However at high current density this trend is replaced by a gradual increase in water content. This change in trend is not observed at all for the 50%RH cases. This difference is possibly caused by two reasons: one is local current density distribution; the other is local heating by fuel cell waste heat generation. Note that the probed water thickness measures the contributions from the channel space and other components such as GDLs and MEAs. For fully humidified cases, the local current is more determined by the oxygen concentration, therefore a higher local current density appears upstream. As a result, the upstream water contents in the MEA and GDLs can be higher than downstream. Because water accumulates in the gas channel down the flow, a trend of a decrease in the overall water thickness followed by an increase will be yielded, as observed in the neutron imaging result. Because of the waste heat generation by the fuel cell, part of liquid water upstream can be evaporated (see Refs. [26,36]). This is more severe for higher current density where more waste heat is generated. Thus, as the overall current density increases, the initial decrease in the local water thickness is diminished or even reverse. For the 1.6 A/cm^2 case, only a gradual increase in water thickness is shown in the figure. As to the 50%RH, the local current is also influenced by the water content. A higher local current can appear where the membrane is better hydrated and oxygen supply is relatively sufficient. This may lead to the monotonic increase in water thickness as

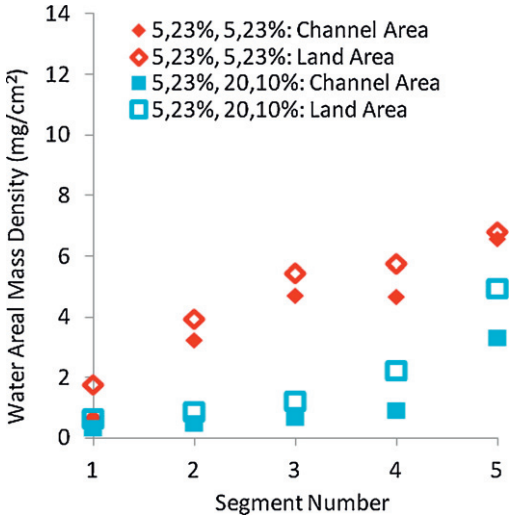

Fig. 11. Water areal density profiles in the projected areas of channel and land regions for cell #1 and #2 at 50% inlet RH and current density of 0.8 A/cm^2.

Author's personal copy

observed. The effect of the local heating may shift the liquid front further downstream, but may not change the increasing trend of water thickness.

Fig. 11 plots the water content profiles in the land and channel projected areas, respectively, for cell #1 and #2. Again as more hydrophobic media is used in the cathode for cell #2, more water is able to transport back to the anode, leading to anode two-phase flow. Comparing with the cathode side, the anode gas flow is slow and insufficient to remove water droplets at the GDL surface [57], therefore exhibiting more liquid coverage over the GDL-channel surface and raising the liquid saturation in diffusion media. The figure also indicates that water content in the land area is higher than that in the channel due to the increased transport resistance under the land.

4. Conclusions

Though in situ neutron imaging, this study examined the effects of several important factors on the water contents in PEM fuel cells, including flow field design, PTFE loading in MPLs/GDLs, relative humidity, flow configuration, and current density. We found that the fuel cell design, GDL/MPL material, and operating condition greatly affected the water level in fuel cells. For the 100% inlet RH case liquid water exists in the entire fuel cell, while for the 50% inlet RH case liquid water appears in part of the fuel cell. In the cases considered, the highest overall water content appears at the current density of 0.4 A/cm^2, possibly due to the lower channel flows and waste heat generation at this lower current. We also found that a more hydrophobic cathode MPL or hydrophilic anode MPL may result in a larger amount of water transporting back to the anode. Higher water contents were found in the quad-serpentine flow field at moderate current densities and in counter-flow configuration as opposed to single-serpentine flow field and co-flow operation, respectively. The water profiles along channels were also provided, indicating liquid water rapidly increases its content after emerging, consistent with previous theoretical analysis. More water content was shown in the land projected area than the channel.

Acknowledgments

This work was supported by the U.S. Department of Energy (DOE) Fuel Cell Technologies (Technology Development Manager: Nancy Garland). This work was also supported by the U.S. Department of Commerce, the NIST Ionizing Radiation Division, the Director's Office of NIST, the NIST Center for Neutron Research, and the Department of Energy through interagency agreement no. DE-AI01-01EE50660. We wish to thank Dr. John Davey of LANL for designing the hardware used in the neutron imaging experiments and Eli Baltic of NIST for help with NIST facility. We would like to acknowledge Peter Wilde of SGL Group for providing the GDL materials. Partial support by the Academic Senate Council on Research, Computing and Library Resources at UCI is gratefully acknowledged.

References

[1] Y. Wang, K.S. Chen, J. Mishler, S.C. Cho, X.C. Adroher, Applied Energy 88 (2011) 981.
[2] Z.H. Wang, C.Y. Wang, K.S. Chen, Journal of Power Sources 94 (2001) 40.
[3] J.H. Nam, M. Kaviany, International Journal of Heat and Mass Transfer 46 (2003) 4595.
[4] U. Pasaogullari, C.Y. Wang, Journal of the Electrochemical Society 151 (2004) A399.
[5] X.G. Yang, F.Y. Zhang, A.L. Lubawy, C.Y. Wang, Electrochemical and Solid-State Letters 7 (2004) A408.
[6] F.Y. Zhang, X.G. Yang, C.Y. Wang, Journal of the Electrochemical Society 153 (2006) A225.
[7] D. Lee, J. Bae, Journal of Power Sources 191 (2009) 390.
[8] C.-Y. Wang, Chemical Reviews 104 (2004) 4727.
[9] A.Z. Weber, J. Newman, Chemical Reviews 104 (2004) 4679.
[10] K. Jiao, X. Li, Progress in Energy and Combustion Science 37 (2011) 221.
[11] V. Gurau, J.A. Mann, SIAM Journal on Applied Mathematics 70 (2009) 410.
[12] K. Tüber, D. Pócza, C. Hebling, Journal of Power Sources 124 (2003) 403.
[13] Y. Wang, Journal of Power Sources 185 (2008) 261.
[14] Y. Wang, C.Y. Wang, K.S. Chen, Electrochimica Acta 52 (2007) 3965.
[15] Z. Qi, A. Kaufman, Journal of Power Sources 109 (2002) 38.
[16] A.Z. Weber, R.M. Darling, J. Newman, Journal of the Electrochemical Society 151 (2004) A1715.
[17] A.Z. Weber, J. Newman, Journal of the Electrochemical Society 152 (2005) A677.
[18] L. Giorgi, E. Antolini, A. Pozio, E. Passalacqua, Electrochimica Acta 43 (1998) 3675.
[19] V.A. Paganin, E.A. Ticianelli, E.R. Gonzalez, Journal of Applied Electrochemistry 26 (1996) 297.
[20] F. Lufrano, E. Passalacqua, G. Squadrito, A. Patti, L. Giorgi, Journal of Applied Electrochemistry 29 (1999) 445.
[21] E. Antolini, R.R. Passos, E.A. Ticianelli, Journal of Applied Electrochemistry 32 (2002) 383.
[22] S. Park, J.-W. Lee, B.N. Popov, Journal of Power Sources 177 (2008) 457.
[23] D.L. Wood, R. Mukundan, R. Borup, ECS Transactions 25 (2009) 1495.
[24] R. Mukundan, J.R. Davey, T. Rockward, J.S. Spendelow, B. Pivovar, D.S. Hussey, D.L. Jacobson, M. Arif, R. Borup, ECS Transactions 11 (2007) 411.
[25] U. Pasaogullari, C.-Y. Wang, K.S. Chen, Journal of the Electrochemical Society 152 (2005) A1574.
[26] Y. Wang, K.S. Chen, Chemical Engineering Science 66 (2011) 3557.
[27] X. Li, I. Sabir, International Journal of Hydrogen Energy 30 (2005) 359.
[28] D. Spernjak, A.K. Prasad, S.G. Advani, Journal of Power Sources 195 (2010) 3553.
[29] Y. Wang, S. Basu, C.Y. Wang, Journal of Power Sources 179 (2008) 603.
[30] Y. Wang, Journal of the Electrochemical Society 156 (2009) B1134.
[31] J.P. Owejan, J.J. Gagliardo, J.M. Sergi, S.G. Kandlikar, T.A. Trabold, International Journal of Hydrogen Energy 34 (2009) 3436.
[32] H. Murakawa, T. Ueda, T. Yoshida, K. Sugimoto, H. Asano, N. Takenaka, K. Mochiki, H. Iikura, R. Yasuda, M. Matsubayashi, Nuclear Instruments and Methods in Physics Research Section A: Accelerators Spectrometers, Detectors and Associated Equipment 605 (2009) 127.
[33] T.A. Trabold, J.P. Owejan, D.L. Jacobson, M. Arif, P.R. Huffman, International Journal of Heat and Mass Transfer 49 (2006) 4712.
[34] R. Satija, D.L. Jacobson, M. Arif, S.A. Werner, Journal of Power Sources 129 (2004) 238.
[35] M.A. Hickner, N.P. Siegel, K.S. Chen, D.N. McBrayer, D.S. Hussey, D.L. Jacobson, M. Arif, Journal of the Electrochemical Society 153 (2006) A902.
[36] M.A. Hickner, N.P. Siegel, K.S. Chen, D.S. Hussey, D.L. Jacobson, M. Arif, Journal of the Electrochemical Society 155 (2008) B294.
[37] J. Zhang, D. Kramer, R. Shimoi, Y. Ono, E. Lehmann, A. Wokaun, K. Shinohara, G. Scherer, Electrochimica Acta 51 (2006) 2715.
[38] J. Park, X. Li, D. Tran, T. Abdel-Baset, D.S. Hussey, D.L. Jacobson, M. Arif, International Journal of Hydrogen Energy 33 (2008) 3373.
[39] J.P. Owejan, T.A. Trabold, D.L. Jacobson, M. Arif, S.G. Kandlikar, International Journal of Hydrogen Energy 32 (2007) 4489.
[40] T. Kim, J. Kim, C. Sim, S. Lee, M. Kaviany, S. Son, M. Kim, Nuclear Instruments and Methods in Physics Research Section A: Accelerators Spectrometers, Detectors and Associated Equipment 600 (2009) 325.
[41] R. Mukundan, Y.S. Kim, T. Rockward, J.R. Davey, B. Pivovar, D.S. Hussey, D.L. Jacobson, M. Arif, R. Borup, ECS Transactions 11 (2007) 543.
[42] Y. Wang, P.P. Mukherjee, J. Mishler, R. Mukundan, R.L. Borup, Electrochimica Acta 55 (2010) 2636.
[43] D. Kramer, J. Zhang, R. Shimoi, E. Lehmann, A. Wokaun, K. Shinohara, G.G. Scherer, Electrochimica Acta 50 (2005) 2603.
[44] K. Yoshizawa, K. Ikezoe, Y. Tasaki, D. Kramer, E.H. Lehmann, G.G. Scherer, Journal of the Electrochemical Society 155 (2008) B223.
[45] I.A. Schneider, D. Kramer, A. Wokaun, G.G. Scherer, Electrochemistry Communications 7 (2005) 1393.
[46] I.A. Schneider, S.V. Dahlen, M.H. Bayer, P. Boillat, M. Hildebrandt, E.H. Lehmann, P. Oberholzer, G.G. Scherer, A. Wokaun, The Journal of Physical Chemistry C 114 (2010) 11998.
[47] I.A. Schneider, M.H. Bayer, S.V. Dahlen, Journal of the Electrochemical Society 158 (2011) B343.
[48] D.S. Hussey, D.L. Jacobson, M. Arif, K.J. Coakley, D.F. Vecchia, Journal of Fuel Cell Science and Technology 7 (2010) 021024.
[49] D. Hussey, J. Mishler, Y. Wang, Private Communication, August 18, 2011.
[50] A.E. Sáez, R.G. Carbonell, AIChE Journal 31 (1985) 52.
[51] Y. Wang, C.-Y. Wang, Journal of the Electrochemical Society 154 (2007) B636.
[52] S. Ge, C.-Y. Wang, Journal of the Electrochemical Society 154 (2007) B998.
[53] Y. Wang, X. Feng, Journal of the Electrochemical Society 156 (2009) B403.
[54] Y. Wang, C.-Y. Wang, Journal of Power Sources 147 (2005) 148.
[55] F.N. Buchi, S. Srinivasan, Journal of the Electrochemical Society 144 (1997) 2767.
[56] R. Hilfer, Physical Review E 58 (1998) 2090.
[57] K.T. Cho, A. Turhan, J.H. Lee, J.S. Brenizer, A.K. Heller, L. Shi, M.M. Mench, Nuclear Instruments and Methods in Physics Research Section A: Accelerators Spectrometers, Detectors and Associated Equipment 605 (2009) 119.